

A Multicomponent Magnetic Proxy for Solar Activity

Harry Warren¹, Linton Floyd², and Lisa A Upton³

¹Naval Research Laboratory

²Interferometrics Inc., USA

³High Altitude Observatory

November 23, 2022

Abstract

We present a new, multicomponent magnetic proxy for solar activity derived from full disk magnetograms that can be used in the specification and forecasting of the Sun's radiative output. To compute this proxy we project Carrington maps, such as the synchronic Carrington maps computed with the Advective Flux Transport (AFT) surface flux transport model, to heliographic cartesian coordinates and determine the total unsigned flux as a function of absolute magnetic flux density. Performing this calculation for each day produces an array of time series, one for each flux density interval. Since many of these time series are strongly correlated, we use principal component analysis to reduce them to a smaller number of uncorrelated time series. We show that the first few principal components accurately reproduce widely used proxies for solar activity, such the the 10.7\,cm radio flux and the Mg core-to-wing ratio. This suggests that these magnetic time series can be used as a proxy for irradiance variability for emission formed over a wide range of temperatures.

A Multicomponent Magnetic Proxy for Solar Activity

Harry P. Warren¹, Linton E. Floyd², and Lisa A. Upton²

¹Space Science Division, Naval Research Laboratory, Washington, DC 20375 USA

²Space Systems Research Corporation, Alexandria, VA, 22314, USA

Key Points:

- A new magnetic proxy for solar activity is presented
- The new magnetic proxy is well correlated with existing proxies

8 Abstract

9 We present a new, multicomponent magnetic proxy for solar activity derived from
 10 full disk magnetograms that can be used in the specification and forecasting of the
 11 Sun’s radiative output. To compute this proxy we project Carrington maps, such as
 12 the synchronic Carrington maps computed with the Advective Flux Transport (AFT)
 13 surface flux transport model, to heliographic cartesian coordinates and determine the
 14 total unsigned flux as a function of absolute magnetic flux density. Performing this
 15 calculation for each day produces an array of time series, one for each flux density
 16 interval. Since many of these time series are strongly correlated, we use principal
 17 component analysis to reduce them to a smaller number of uncorrelated time series.
 18 We show that the first few principal components accurately reproduce widely used
 19 proxies for solar activity, such the the 10.7 cm radio flux and the Mg core-to-wing ratio.
 20 This suggests that these magnetic time series can be used as a proxy for irradiance
 21 variability for emission formed over a wide range of temperatures.

22 Plain Language Summary

23 Proxies for solar activity are often used to extend solar irradiance measurements
 24 in time or forecast future variability. Widely used proxies, such as the 10.7 cm radio
 25 flux, can include emission formed from different mechanisms, which limits their ability
 26 to accurately reproduce some irradiance time series. Other proxies, such as the Mg
 27 core-to-wing ratio, perform better, but are taken from different space instruments,
 28 whose long-term calibration can be difficult to understand. In this paper we show
 29 how to use images of the solar photospheric magnetic field to create a multicomponent
 30 proxy for solar activity that overcomes some of the limitations of existing proxies.

31 1 Introduction

32 Information on the solar spectral irradiance and its variability is needed to under-
 33 stand the state of the Earth’s upper atmosphere. Ideally, the spectral irradiance
 34 at all wavelengths would be monitored continuously. Since this must be done from
 35 space, most spectral irradiance measurements are available for only for limited inter-
 36 vals of time. To extrapolate irradiance measurements to other times, proxies for solar
 37 activity are used in a regression model. Furthermore, forecasts of solar activity fo-
 38 cus on forecasting the proxies rather than forecasting the spectral irradiance directly.
 39 Thus proxies for solar activity play an important role in understanding the near-Earth
 40 environment.

41 The 10.7 cm radio flux (F10, Tapping (2013)) is a widely used proxy for solar
 42 activity. This ground-based radio measurement has been made almost daily since the
 43 late 1940’s and appears to be very stable. A long time series of radio measurements at
 44 several frequencies is also available from the Nobeyama Radio Observatory (Tanaka et
 45 al., 1973). Comparisons of F10 and irradiance time series, however, often show a non-
 46 linear dependance and regression models often use F10 and its 81-day running mean as
 47 independent variables in a multiple linear regression to improve the correlation (Lean
 48 et al., 2009). The Mg core-to-wing ratio (Heath & Schlesinger, 1986), which uses the
 49 properties of the Mg II h and k doublet near 280 nm, is another widely used proxy.
 50 This emission must be observed from space and the extended core-to-wing time series
 51 stitches together measurements from a number of different instruments, each of which
 52 has different capabilities.

53 It has long been recognized that the Sun’s radiative output is strongly correlated
 54 with the magnetic field (Gurman et al., 1974), which has been measured extensively
 55 over the past 50 years using both ground based and space based instruments. Further-
 56 more, almost all of these measurements are spatially resolved, yielding information

57 on the distribution of magnetic flux on the solar surface. Finally, the evolution of
 58 the surface magnetic field is well described by models, which provide a physics-based
 59 framework for forecasting solar activity. Surprisingly, there are only a few studies
 60 which investigate the use of the magnetic field as a proxy for solar activity (e.g.,
 61 Henney et al. (2012, 2015)).

62 In this paper we develop a new, multicomponent magnetic proxy for use in the
 63 specification and forecasting of the Sun’s radiative output. As we will see, the multi-
 64 component nature of this proxy is important for accurately modeling emission formed
 65 at many different temperatures in the solar atmosphere, something that is difficult with
 66 proxies such as F10. This work is primarily based on synchronic Carrington maps com-
 67 puted with the Advective Flux Transport (AFT) model (Upton & Hathaway, 2014b,
 68 2014a, 2018), which assimilates observations from Michelson Doppler Imager (MDI)
 69 and The Helioseismic and Magnetic Imager Investigation (HMI) instruments (Scherrer
 70 et al., 1995, 2012). Using the magnetic field determined from a surface flux transport
 71 model makes it easy to use the proxy for forecasting and also addresses some of the
 72 limitations of magnetic field measurements made near the solar limb.

73 2 Magnetic Flux Histograms and Time Series

74 The AFT model describes how the radial component of the magnetic field on the
 75 solar surface is advected by supergranular diffusion, differential rotation, and merid-
 76 ional flow. The unique aspect of the model is its use of a time-dependent velocity
 77 pattern (Hathaway et al., 2010) in place of an ad hoc diffusion term to account for
 78 the transport of magnetic flux by supergranular motions. For this work we use AFT
 79 runs that are updated periodically with an observed line-of-sight magnetogram. The
 80 assimilated data is weighted to emphasize observations near disk center, so the AFT
 81 maps are dominated by the actual measurements in the region facing the Earth.

82 The observed magnetograms are taken from the Michelson Doppler Imager (MDI)
 83 on the Solar and Heliospheric Observatory (SoHO), which operated from 1996 to 2011,
 84 and the Helioseismic and Magnetic Imager (HMI, Scherrer et al. (2012)) on the Solar
 85 Dynamics Observatory (SDO), which began operations in 2010. For the HMI data,
 86 hourly synoptic data is assimilated. For MDI the synoptic data is available every 96
 87 minutes. The magnetic field measurements from the two instruments have some subtle
 88 differences (Liu et al., 2012), which are accounted for before the data is assimilated.
 89 Because of the extended loss of contact with SoHO in 1998, we begin our analysis on
 90 April 1, 1999, transition to using AFT maps based on HMI on June 1, 2010, and end
 91 our analysis on December 31, 2020. We computed a total 7947 AFT magnetograms
 92 during this time, one for each day. The AFT calculation takes about one day of actual
 93 time for each year of the simulation.

94 An example Carrington map from AFT is shown in Figure 1. Here we also
 95 show a projection of the Carrington map to heliographic cartesian coordinates and a
 96 corresponding observed HMI magnetogram. Because the model is updated regularly,
 97 the Earth-facing side of the Sun heavily weighted by the data and the images are
 98 very similar. The primary advantage of using the AFT model instead of the observed
 99 magnetic flux is that the field at the limb is less noisy and does not suffer from “canopy”
 100 effects, where strong flux at the limb has the wrong sign because of projection effects.
 101 One limitation of the model is that flux that has emerged on the far side and has
 102 just rotated over the limb is not fully assimilated immediately. Both of these effects,
 103 though subtle, are evident in this example.

104 Anticipating comparisons with F10, which is measured between 17 and 23 UT, we
 105 compute the magnetogram images for 16 UT, the closest time for which AFT snapshots
 106 are available. Perhaps the simplest approach to constructing a proxy for solar activity

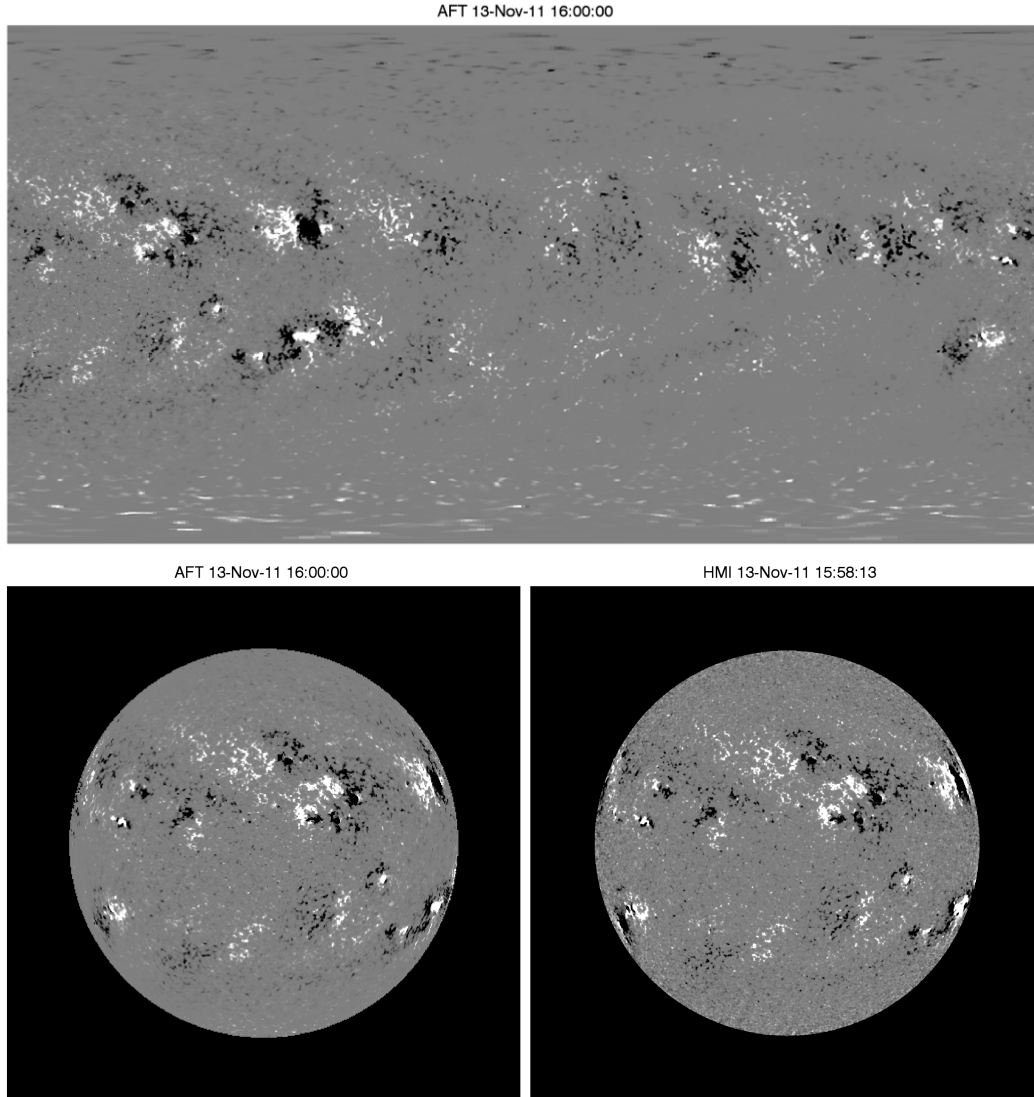


Figure 1. (top panel) An example snapshot from the AFT calculation of the surface magnetic flux. (bottom left) The AFT Carrington map projected to heliographic cartesian coordinates. (bottom right) An HMI magnetogram from approximately the same time. The magnetogram has been smoothed to the spatial resolution of the AFT image and corrected to account for the line-of-sight projection. The AFT and HMI images are generally very similar, but there are some differences at the limb. Because of project effects, strong flux at the west limb has the wrong sign. Newly emerged flux at the east limb has not been fully assimilated into the model.

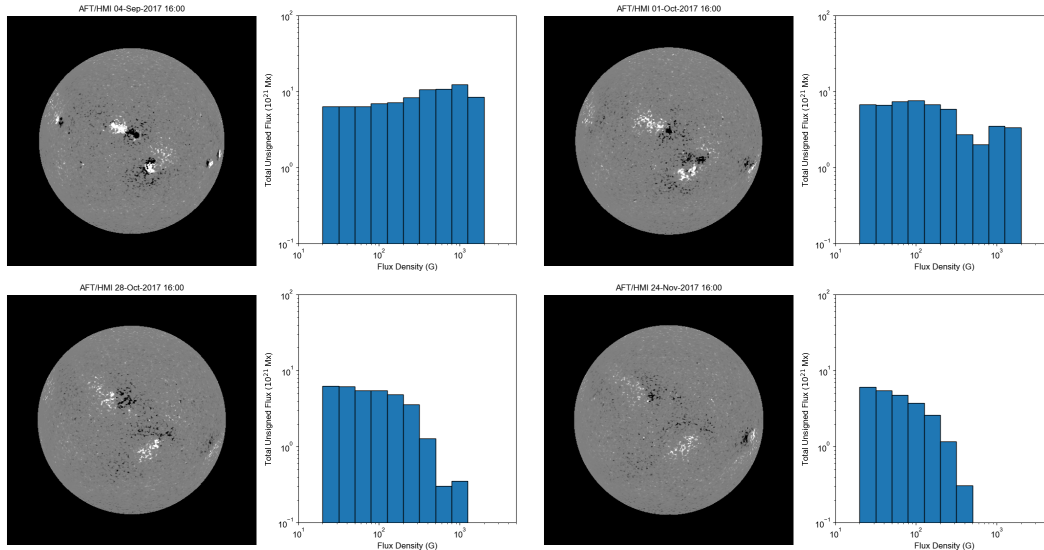


Figure 2. Example histograms of total unsigned magnetic flux as a function of magnetic flux density for four days in 2017. The magnetograms were computed from the AFT maps. The strong temporal variability of the largest fluxes is evident.

107 from these images would be to compute the total unsigned flux for each image, that
 108 is, the sum of the absolute magnitude of the flux density in each pixel multiplied by
 109 the pixel area. The relationship between the radiance and the magnetic field, however,
 110 can be complex. The strong magnetic fluxes found in sunspots, for example, rarely
 111 produce bright emission (e.g., Tiwari et al., 2017). Similarly, the weakest quiet sun
 112 fluxes are always present and unlikely to be strongly correlated with variations in the
 113 irradiance. One might imagine defining different ranges of fluxes to represent different
 114 components of variability (e.g., quiet Sun, active network, active region), but it is not
 115 clear how to define these boundaries.

116 For this work we adopt a two step procedure that circumvents these problems.
 117 We first construct histograms of the unsigned magnetic flux as a function of flux density
 118 for each day. We then perform principal component analysis (PCA) on the resulting
 119 time series to reduce them to a more manageable size. Recall that PCA is a technique
 120 for reducing the dimensionality of a dataset by defining a new orthonormal basis that
 121 is ordered by information content. Typically, the first few components account for a
 122 large percentage of the variance in the data.

123 Figure 2 illustrates the calculation of histograms for four days, each approxi-
 124 mately one solar rotation apart, in late 2017 when several large active regions emerged
 125 on the disk and decayed over time. Here 10 logarithmically spaced bins between 20
 126 and 2000 G have been chosen to compute these distributions. The lower value does
 127 not include 0 because very weak fluxes are difficult to measure. The noise level in the
 128 magnetograms is estimated to be about 10 G (Yeo et al., 2014), and is likely to be
 129 higher near the limb.

130 Time series for selected bins are shown in Figure 3. These time series of total
 131 unsigned flux show modulation over both rotational and solar cycle time scales. The
 132 amplitude of this modulation increases with increasing magnetic flux density. As one
 133 would expect, the fluxes in adjacent bins are strongly correlated, indicating that some
 134 of the information in these time series is redundant.

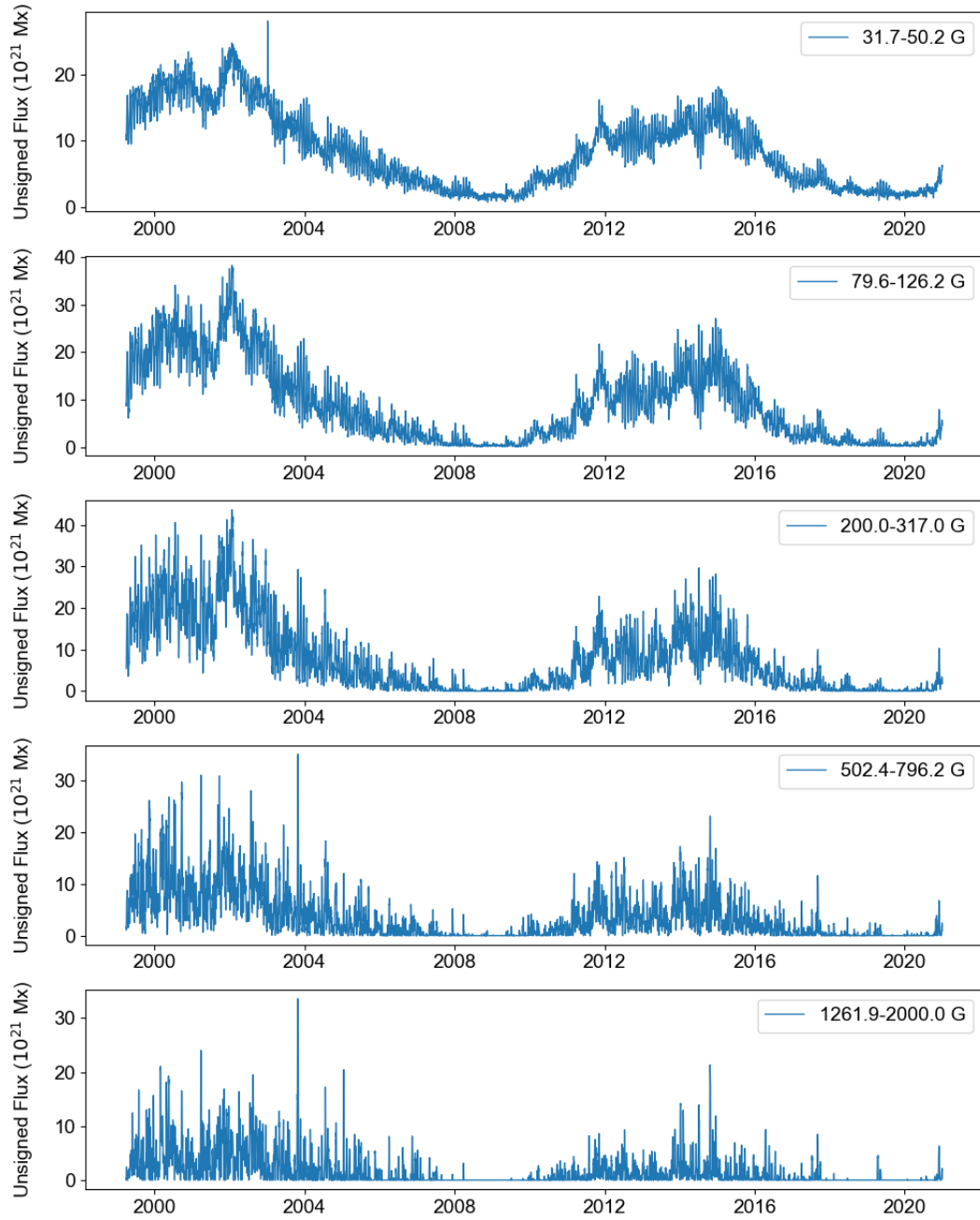


Figure 3. Time series of the total unsigned magnetic flux (flux density times pixel area in units of 10^{21} Mx) for selected flux density bins.

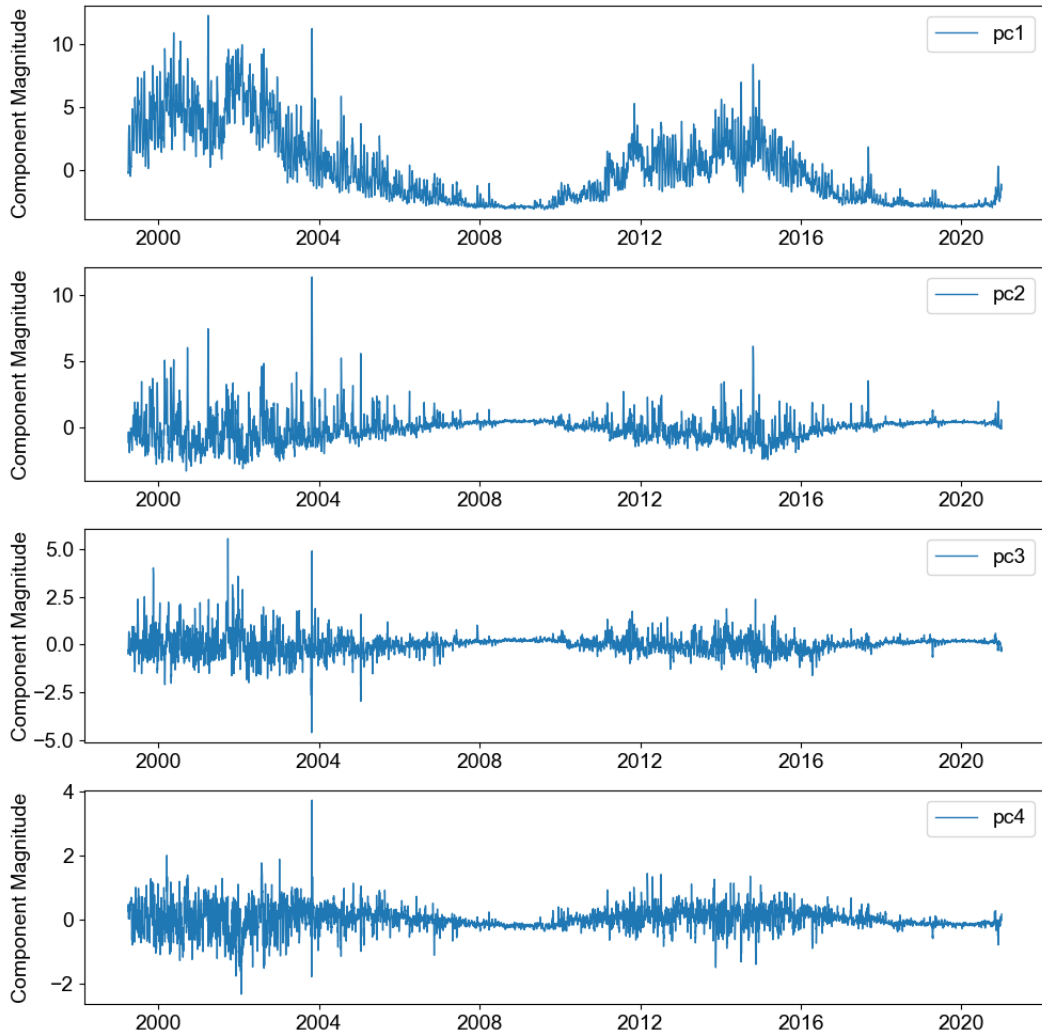


Figure 4. Time series of the first four principal components. Together, these components account for 99% of the variance in the original time series. Note that each time series has been normalized so that the components are dimensionless.

135 We use the PCA package from scikit-learn (Pedregosa et al., 2011) to compute
 136 the principle components of the magnetic time series. The first four components, which
 137 account for 85, 95, 98, and 99% of the variance in the original time series of magnetic
 138 fluxes, are shown in Figure 4. Note the the magnetic time series are scaled to have
 139 zero mean and unit variance before the PCA decomposition is computed. Thus the
 140 components are dimensionless.

141 3 Example Applications

142 The processed magnetic time series shown in Figure 4 can be used to model the
 143 temporal variability of solar irradiance time series. To illustrate this application we
 144 show that the magnetic time series can capture the evolution of F10, the Mg core-
 145 to-wing ratio, several frequencies observed at the Nobeyama Radio Observatory, and
 146 several irradiance time series from EUV Variability Experiment (EVE, Woods et al.
 147 (2012)) on *SDO*. For all of these time series we will perform a simple multiple linear
 148 regression of the form

$$\text{Irradiance}(t) = c_0 + \sum_{i=1}^4 c_i M_i(t), \quad (1)$$

149 where $M_i(t)$ is a PCA component of the magnetic time series. We use the Python
 150 `statsmodel` package (Seabold & Perktold, 2010) to perform these fits. The sources of
 151 these data are described in Section 5.

152 3.1 F10

153 We fit all of the available magnetic data and F10 to Equation 1. In Figure 5
 154 we show a time series of the observed F10 and the values inferred from the fit. Also
 155 shown are the a correlation between the modeled and observed values, the residuals
 156 as a function of time, and a histogram of the residuals. To highlight the variation of
 157 the irradiance over a solar rotation, time series for smaller time ranges are also shown
 158 in Figure 5.

159 The model fits the observations of F10 very well. The correlation between the
 160 modeled and observed values is 0.98. The residuals are relatively small, with a standard
 161 deviation of 6.4%. The residuals are generally biased towards larger values, where the
 162 model systematically under-predicts the observations. Some of these differences may
 163 be due to very large sunspots that influence the F10 measurements, but are not well
 164 captured by the magnetograms (e.g., September 2017). Flares could also influence the
 165 F10 measurements more than the magnetograms. Close inspection of the residuals
 166 suggests an unexpected secular trend between 2004 and 2015, which seems to resume
 167 around 2016. As we will see, this pattern is evident in some of the other irradiance
 168 time series. We will discuss this in some detail in Section 4.

169 We fit F10 using progressively more principle components to test the impact
 170 of increasing model complexity on goodness of fit. As noted earlier, The first four
 171 components account for 85, 95, 98, and 99% of the variance in the original time series.
 172 Using only the first component yields a correlation of 0.97 and a dispersion in the
 173 residuals of 7.2%. Adding the remaining components yields correlations of 0.97, 0.98,
 174 and 0.98. For the dispersion the results are 7.1%, 6.8%, and 6.4%. Thus, the first
 175 two components account for the the vast majority of the variation in the observed
 176 irradiance time series.

177 3.2 Mg Core-to-Wing

178 The fit of the Mg core-to-wing ratio to the magnetic time series is shown in
 179 Figure 6. The format of the figures is identical to Figure 5. The magnetic model,

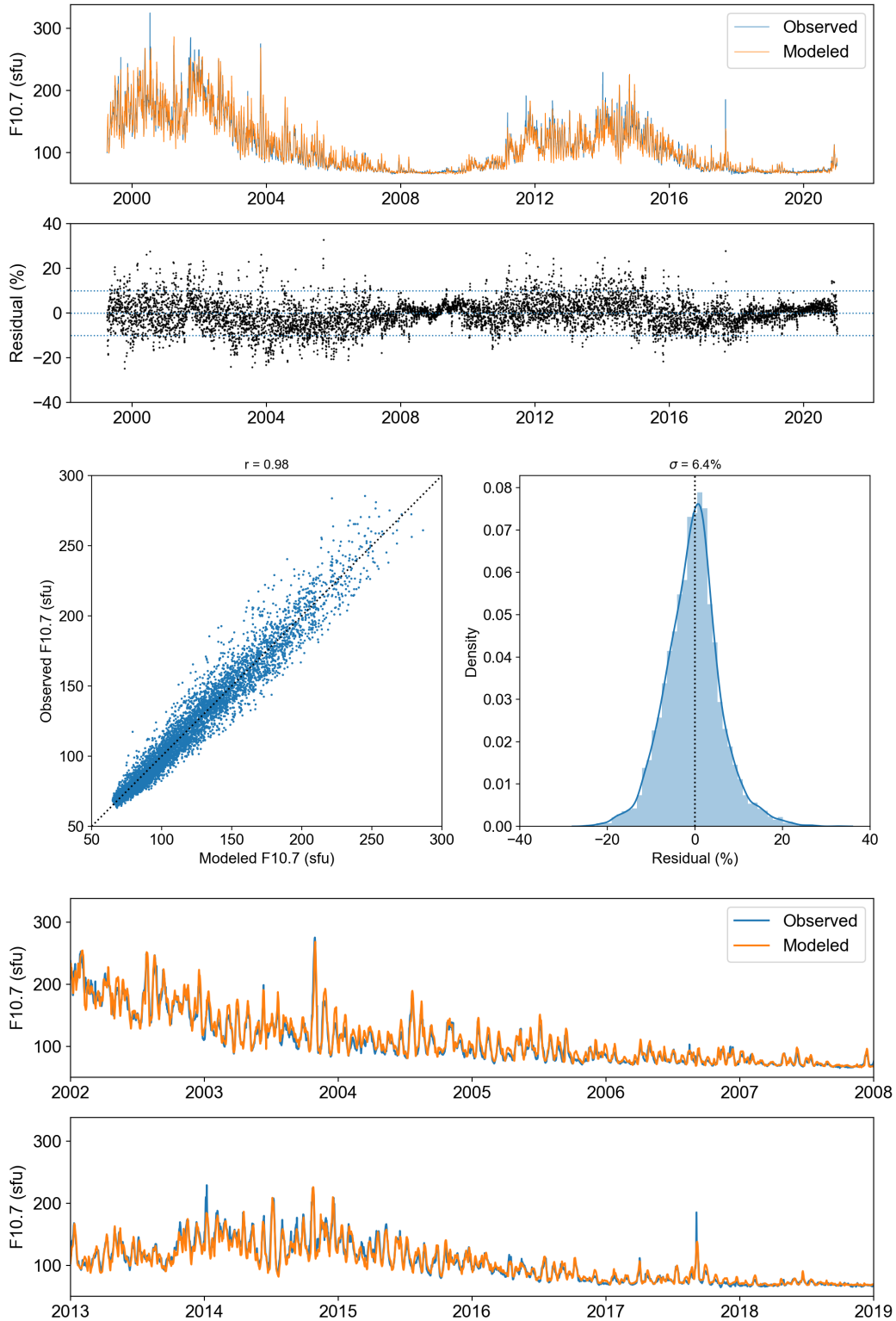


Figure 5. Results from a multiple linear regression of the magnetic flux proxy to F10. The top panels show the observed and modeled values and the residuals. The middle panels show a scatter plot of the observed and modeled value and the distribution of the residuals. The bottom panels show the observed and modeled time series over limited intervals. The model reproduces the observed values very well.

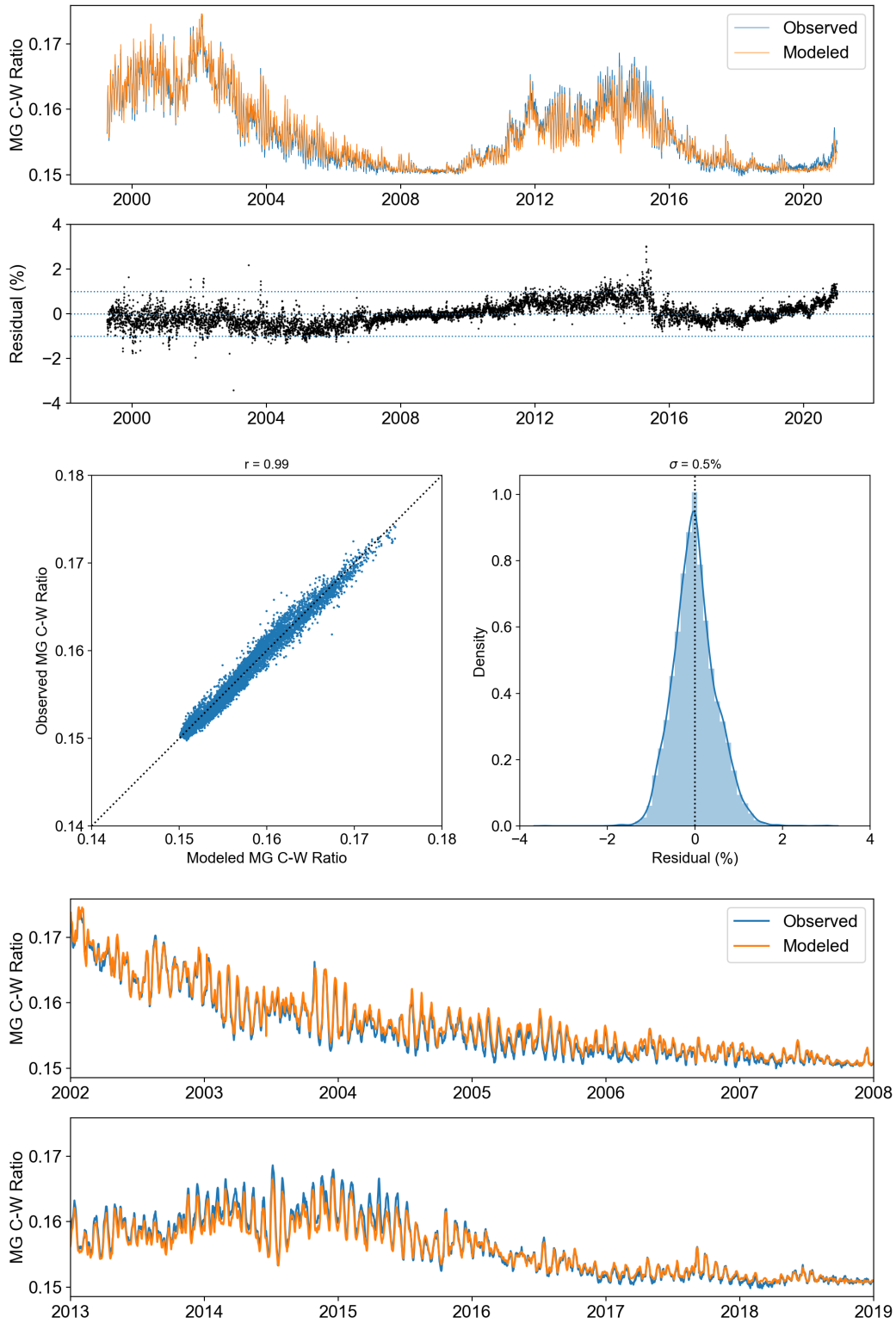


Figure 6. Results from a multiple linear regression of the magnetic flux proxy to the Mg core-to-wing ratio. The format is identical to Figure 5

Table 1. Fitting Metrics for EVE Irradiance Time Series

	Residual (%)			Correlation		
	304	195	360	304	195	360
F10	3.5	11.8	28.8	0.91	0.85	0.96
Mg	2.3	8.3	31.3	0.96	0.82	0.97
<i>B_{PCA}</i>	2.5	7.8	29.4	0.96	0.93	0.97

180 however, fits Mg better than F10. The correlation is higher and the residuals are
 181 smaller. The residuals shown in Figure 6 show the secular trends that were alluded
 182 to in the discussion on the fits to F10. Again, we will discuss possible explanation for
 183 this in Section 4.

184 3.3 Nobeyama Radio Observatory

185 Measurements of the Sun’s radio emission at several frequencies have been mon-
 186 itored at the Toyokawa and Nobeyama radio polarimeters since the 1950’s (Tanaka et
 187 al., 1973), creating long time series that are useful for irradiance modeling. Observa-
 188 tions at 30, 15, 8, and 3.2 cm are available. Dudok de Wit et al. (2014) show that the
 189 30 cm flux is better for modeling the thermosphere-ionosphere system. The fit of the
 190 30 cm (1.0 GHz) signal to the magnetic time series is shown in Figure 7. The corre-
 191 lation and residuals are similar to those seen in the fit to F10. Here the correlation
 192 between the model and the observation is 0.98 and the dispersion in the residuals is
 193 7.3%.

194 3.4 EVE

195 As a final application we consider fits of irradiance time series observed with EVE
 196 to the magnetic proxy. We have chosen lines formed at three different temperatures in
 197 the solar atmosphere: He II 304 Å, Fe XII 195 Å, and Fe XVI 360 Å. The first two lines
 198 were observed with the short wavelength range of EVE (“MEGS-A”), which ceased
 199 operations in May of 2014.

200 The observed and modeled time series, scatter plots, and histograms are shown
 201 in Figures 8, 9, and 10. The fit to He II 304 Å is very good, with small residuals over
 202 the entire time period, similar to the results from the Mg core-to-wing ratio. The fits
 203 to the other wavelengths are not as good. Fe XII 195 Å shows some relatively large
 204 discrepancies early in the EVE mission, where the model is systematically lower than
 205 the observations. The residuals are about a factor of 3 higher than those for He II
 206 304 Å and have a large tail to negative values. The residuals for Fe XVI 360 Å are
 207 larger still, reaching values of $\pm 100\%$. This is somewhat misleading, however. Fe XVI
 208 is formed at a high temperature and the signal in this line becomes very weak during
 209 solar minimum. Figure 10 shows a clear trend towards lower residuals during periods
 210 of higher solar activity. Still, even if we restrict the calculation to the core of the
 211 distribution, the residuals are about 10 times higher than they are for He II 304 Å. All
 212 of these irradiance time series show a linear relationship between the observed and
 213 modeled fluxes.

214 These fits of the magnetic proxy to the EVE irradiance time series can be com-
 215 pared with the more traditional fits to F10 or the Mg core-to-wing ratio. This is shown
 216 in Figure 11, where scatter plots of modeled and observed irradiances are displayed.
 217 The residuals from these fits show that the magnetic flux proxy performs as well as
 218 the Mg core-to-wing ratio and better than F10.

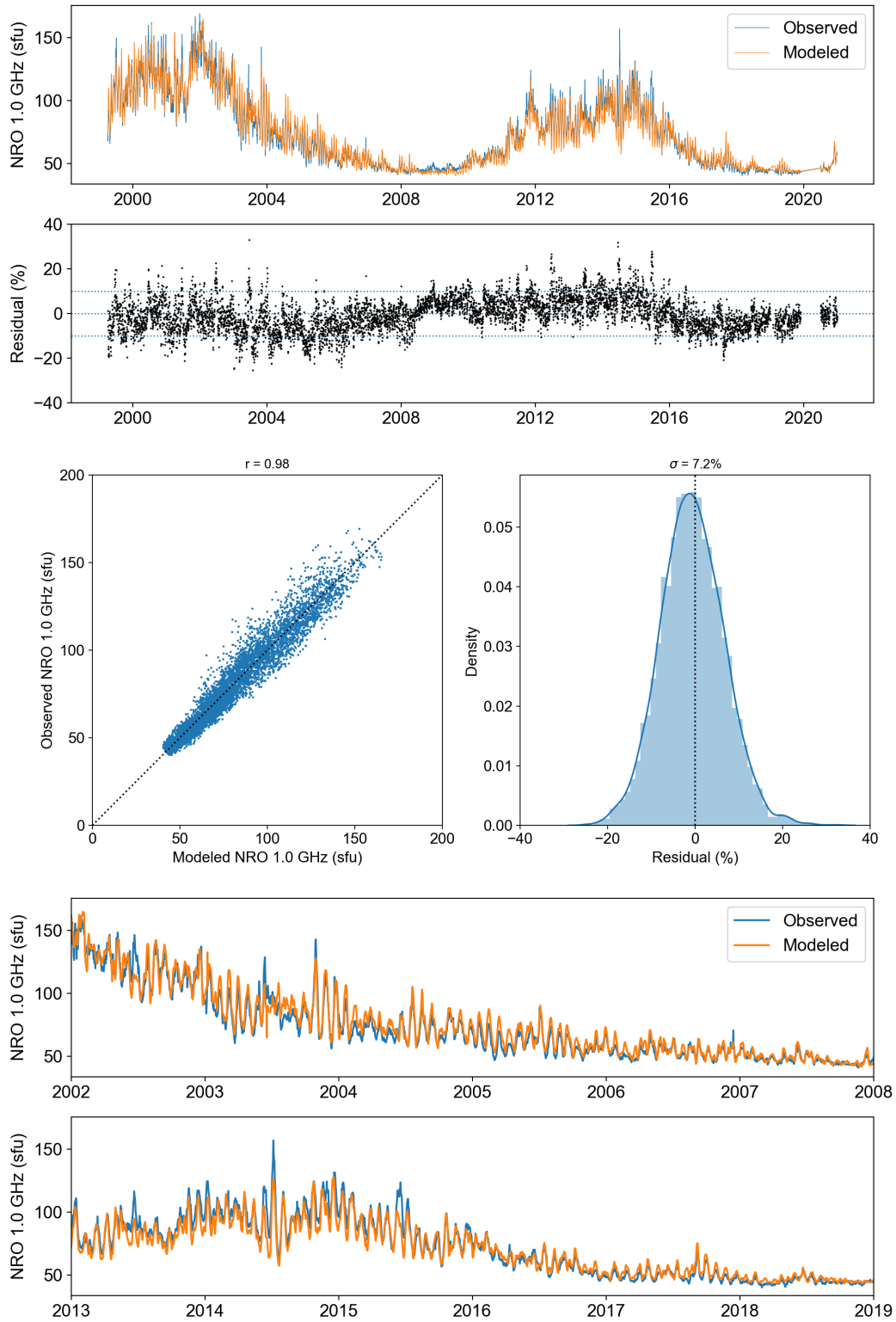


Figure 7. Results from a multiple linear regression of the magnetic flux proxy to the 1 GHz signal measured by the Nobeyama Radio Observatory. The format is identical to Figure 5.

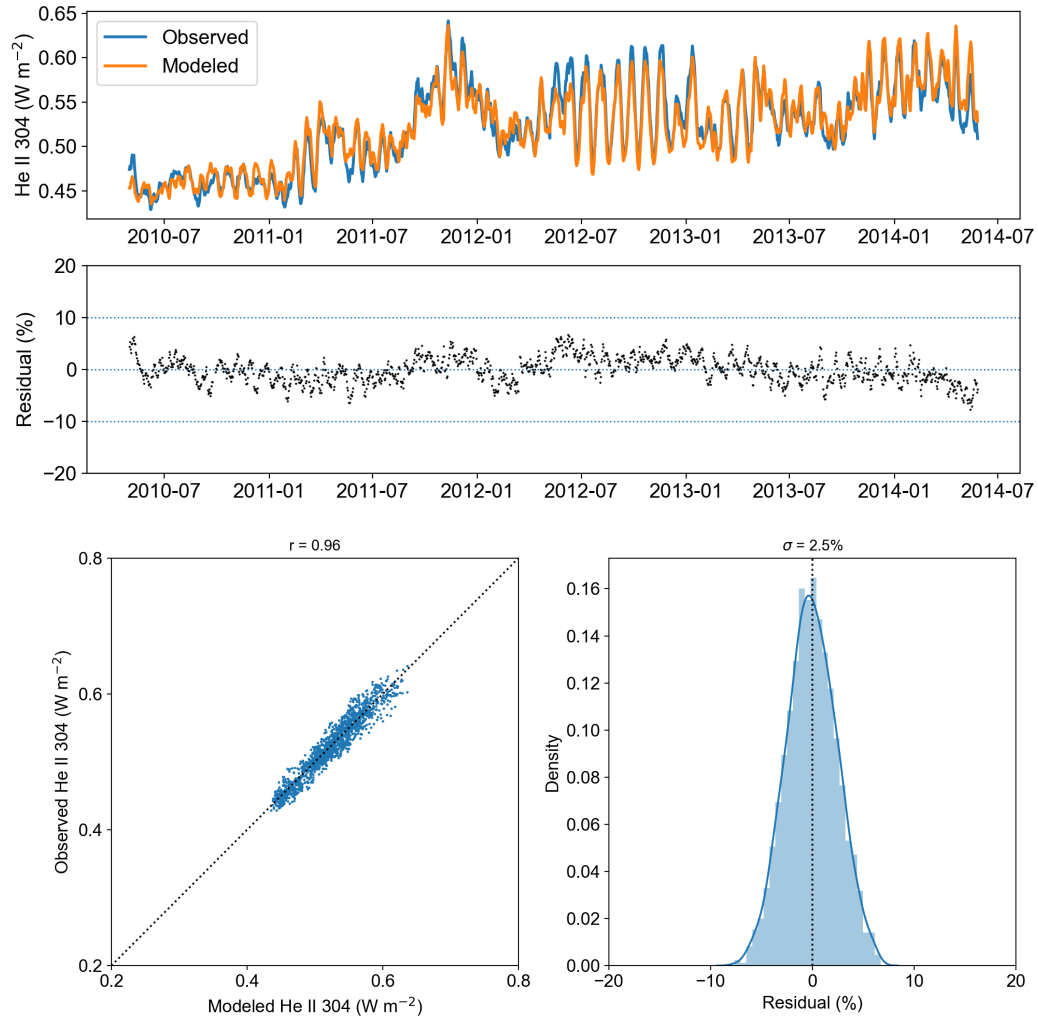


Figure 8. Results from a multiple linear regression of the magnetic flux proxy to the He II 304 Å irradiance observed with EVE.

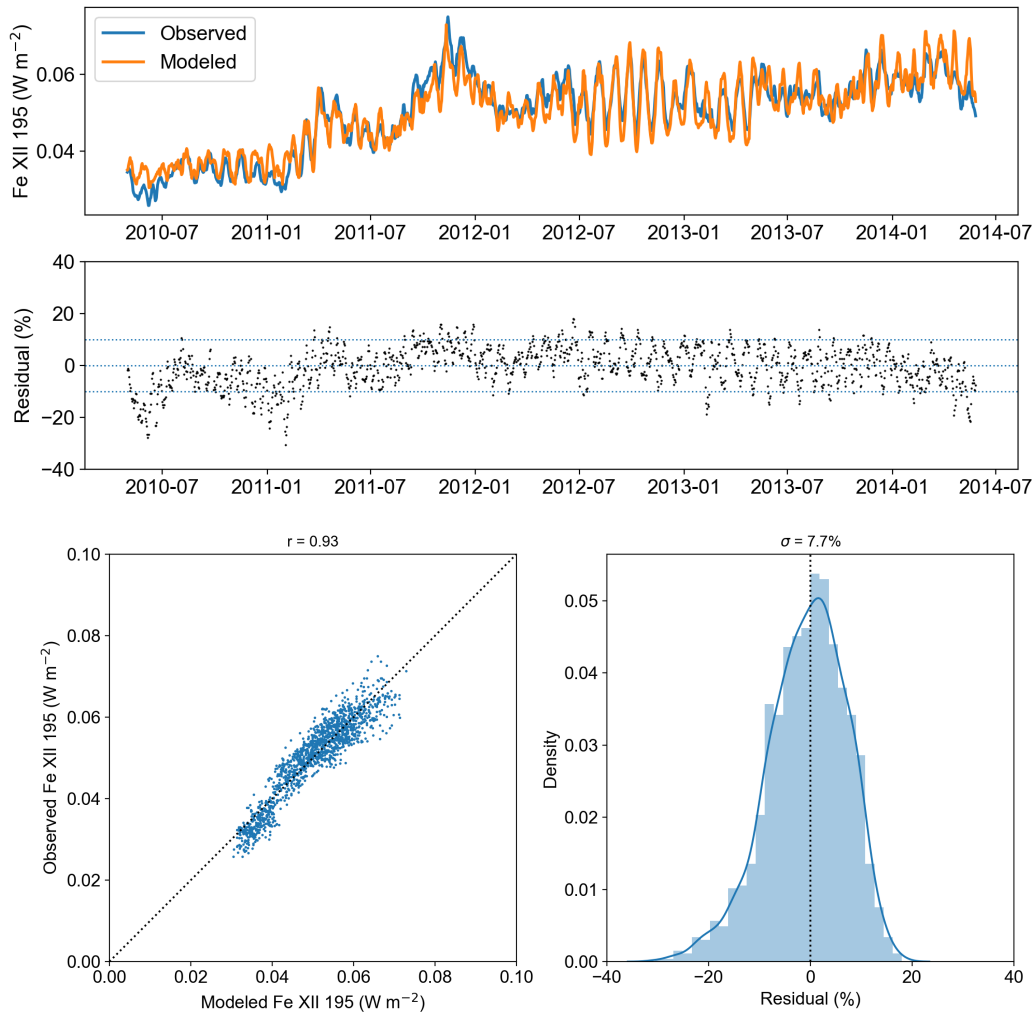


Figure 9. Results from a multiple linear regression of the magnetic flux proxy to the Fe XII 195 Å irradiance observed with EVE. The format is identical to Figure 5.

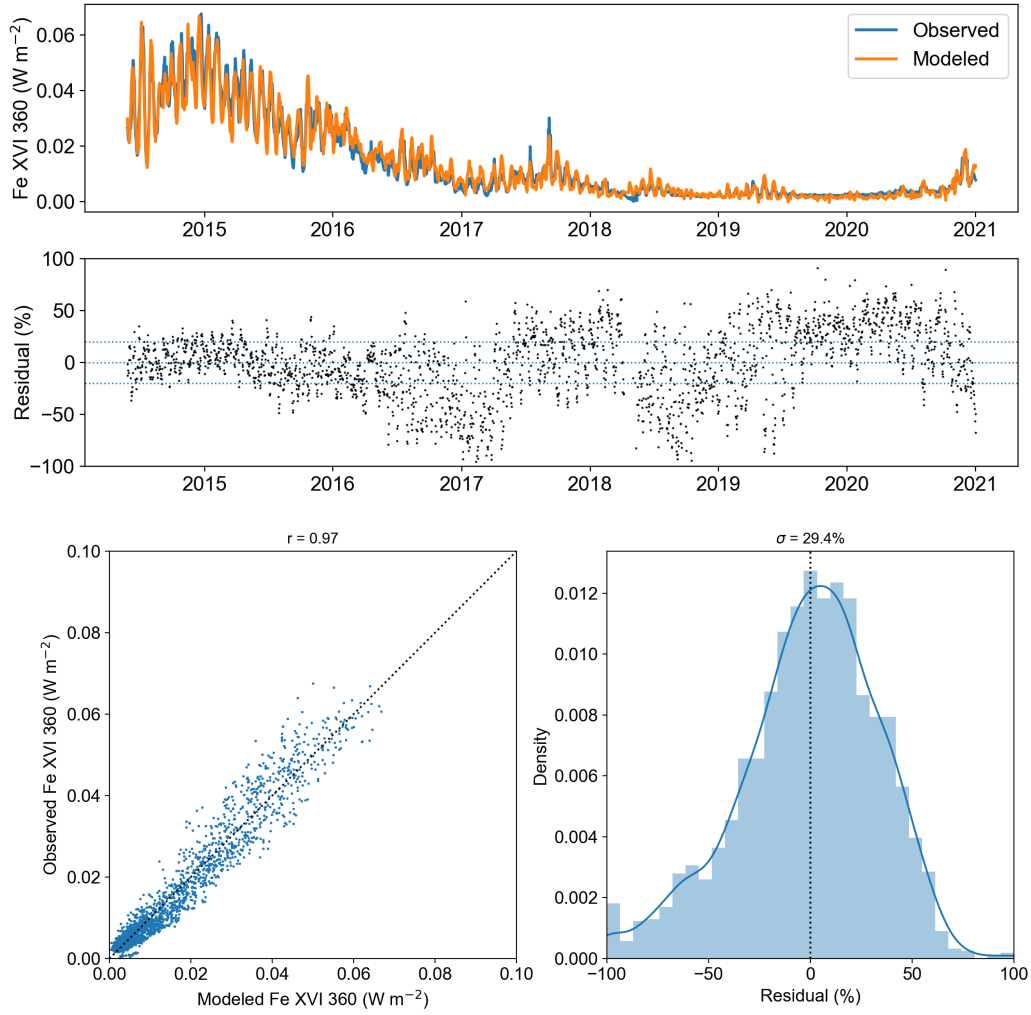


Figure 10. Results from a multiple linear regression of the magnetic flux proxy to the Fe XVI 360 Å irradiance observed with EVE.

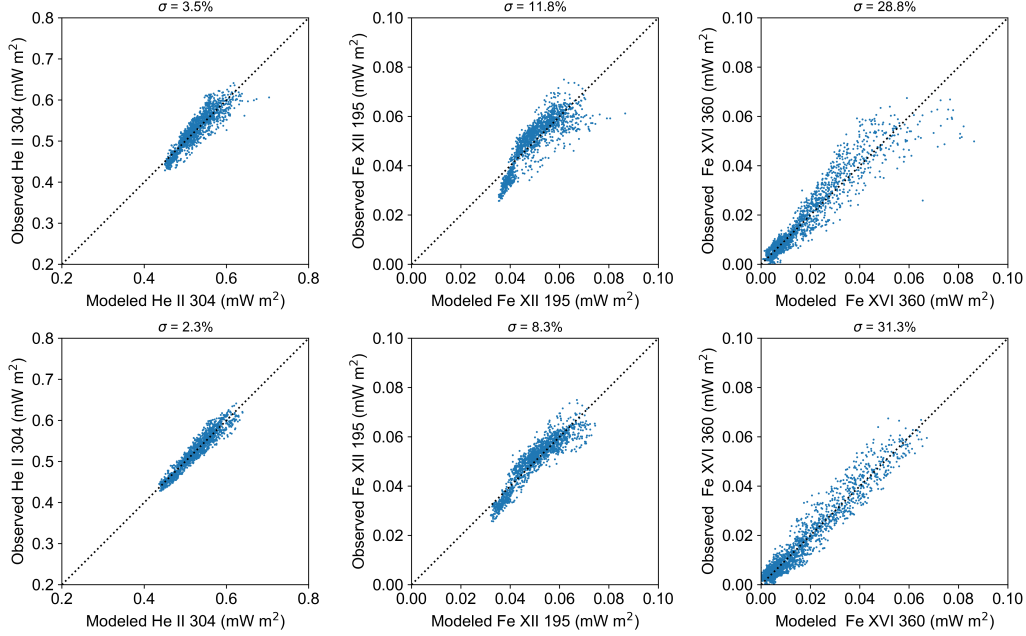


Figure 11. Scatter plots of modeled and observed EVE irradiances using the F10 and Mg core-to-wing ratio as proxies for solar activity.

219

4 Summary and Discussion

220

221

222

223

We have presented a new proxy for solar activity that can be used in the specification and forecasting of the solar irradiance. We have shown that this proxy can be used to accurately model other proxies for solar activity and irradiance time series formed at different layers in the solar atmosphere.

224

225

226

227

228

229

230

231

232

233

234

235

236

237

The secular trends seen in the residuals between the data and the model fits are unexpected. These trends are most clearly seen in the analysis of the Mg core-to-wing ratio data (Figure 6) and are largely absent in the fits to the EVE irradiances. To investigate the possible origins of these trends we compared the flux time series derived from the AFT images with those from the HMI observations. For the largest flux densities, above about 80 G, these time series are very similar. At smaller flux densities, however, these time series show non-trivial differences. Unfortunately, the origin of these differences is unclear. It seems that the AFT simulation modifies these weak fluxes in a way that is inconsistent with the observations. Since the assimilation of the data into the AFT model is weighted towards disk center, it is possible for these inconsistencies to persist. Of course, weak fluxes near the limb are the most difficult to measure, making it difficult to identify the origin of these differences. Ultimately, the weakest fluxes have the smallest effect on the irradiance time series and the residuals are acceptably small.

238

239

240

241

242

243

244

245

This magnetic proxy has several advantages over previous proxies. The use of spatially resolved magnetograms allows for multiple components to be defined that can reproduce emission formed at many different temperatures. While the AFT model used for this work made use of space-based magnetogram measurements, magnetograms can also be observed from the ground. The use of ground-based magnetograms should make it much easier to obtain consistent measurements over long periods of time, although this remains to be demonstrated, as long-term financial support needs to be provided for a distribution of ground based observatories. The Global Oscillation

246 Network Group (GONG) is an example of such a network, and a next generation
247 GONG would provide additional important capabilities (Hill et al., 2019). Finally,
248 the evolution of surface magnetic flux is well described by models such as AFT, which
249 provides a physics-based framework for forecasting solar activity.

250 This work suggests several future research directions. For example, spatially
251 resolved magnetogram measurements from the Mount Wilson Observatory (MWO)
252 extend back to the early 1970's (Pevtsov et al., 2021) and our histogram analysis
253 could be applied to these data to create a much longer magnetic proxy time series.
254 Additionally, the skill of flux transport models in forecasting solar activity needs to
255 be compared with simpler, statistical methods (e.g., Warren et al. (2017)). It seems
256 likely that flux transport models will be limited by a lack of knowledge of both past
257 far-side and future near-side flux emergence. The use of helioseismology or images
258 from STEREO could provide a means for addressing this problem and improving flux
259 transport simulations.

260 5 Data Availability Statement

261 We have made all of the projected magnetograms derived from the AFT flux
262 transport simulation publicly available as standard FITS files on Zenodo (10.5281/zeno-
263 do.5094741). The total volume of data is about 11 GB. The projected magnetograms
264 are derived from a much larger set of AFT Carrington maps of the surface magnetic
265 field, which are not included.

266 All of the data products derived from the magnetograms are available on a
267 GitHub repository

268 <https://github.com/USNavalResearchLaboratory/MagneticProxy>

269 The derived data products include the histograms of magnetic flux for each day, the
270 PCA time series derived from the histograms, and the fit parameters for the PCA
271 model of F10, Mg core-to-wing, the Nobeyama Radio Observatory time series, and
272 the EVE irradiance time series. Additionally, routines for reading these derived data
273 products are also available in the repository. The routines are written in Python and
274 can be run with a recent distribution of Anaconda.

275 The F10.7 radio flux data were downloaded from

276 ftp://ftp.seismo.nrcan.gc.ca/spaceweather/solar_flux/daily_flux_values/fluxtable.txt

277 The Mg core-to-wing Ratio data were downloaded from

278 <http://www.iup.uni-bremen.de/gome/solar/MgII.composite.dat>

279 The Nobeyama Radio Polarimeter data were downloaded from

280 <https://solar.nro.nao.ac.jp/norp/data/daily/>

281 The EVE/SDO data were downloaded from

282 https://lasp.colorado.edu/lisird/data/sdo_eve_lines_l3/

283 All of these data were converted into csv files, which are included in the repository.

284 Acknowledgments

285 This work was supported by NASA's Solar Irradiance Science Team (SIST) and Living
286 with a Star (LWS) programs as well as by the Office of Naval Research.

287

References

- 288 Dudok de Wit, T., Bruinsma, S., & Shibasaki, K. (2014, February). Synoptic radio
 289 observations as proxies for upper atmosphere modelling. *J. Space Weather and*
 290 *Space Clim.*, *4*, A06. doi: 10.1051/swsc/2014003
- 291 Gurman, J. B., Withbroe, G. L., & Harvey, J. W. (1974, January). A Comparison
 292 of EUV Spectroheliograms and Photospheric Magnetograms. *Sol. Phys.*, *34*(1),
 293 105-111. doi: 10.1007/BF00149602
- 294 Hathaway, D. H., Williams, P. E., Dela Rosa, K., & Cuntz, M. (2010, December).
 295 The Advection of Supergranules by the Sun's Axisymmetric Flows. *ApJ*,
 296 *725*(1), 1082-1090. doi: 10.1088/0004-637X/725/1/1082
- 297 Heath, D. F., & Schlesinger, B. M. (1986, July). The Mg 280-nm doublet as a mon-
 298 itor of changes in solar ultraviolet irradiance. *J. Geophys. Res.*, *91*(D8), 8672-
 299 8682. doi: 10.1029/JD091iD08p08672
- 300 Henney, C. J., Hock, R. A., Schooley, A. K., Toussaint, W. A., White, S. M., &
 301 Arge, C. N. (2015, March). Forecasting solar extreme and far ultraviolet
 302 irradiance. *Space Weather*, *13*(3), 141-153. doi: 10.1002/2014SW001118
- 303 Henney, C. J., Toussaint, W. A., White, S. M., & Arge, C. N. (2012, February).
 304 Forecasting F_{10.7} with solar magnetic flux transport modeling. *Space Weather*,
 305 *10*, S02011. doi: 10.1029/2011SW000748
- 306 Hill, F., Hammel, H., Martinez-Pillet, V., de Wijn, A., Gosain, S., Burkepile, J., ...
 307 Suematsu, Y. (2019, September). ngGONG: The Next Generation GONG
 308 - A New Solar Synoptic Observational Network. In *Bulletin of the american*
 309 *astronomical society* (Vol. 51, p. 74).
- 310 Lean, J. L., Picone, J. M., & Emmert, J. T. (2009, July). Quantitative forecasting of
 311 near-term solar activity and upper atmospheric density. *Journal of Geophysical*
 312 *Research (Space Physics)*, *114*(A7), A07301. doi: 10.1029/2009JA014285
- 313 Liu, Y., Hoeksema, J. T., Scherrer, P. H., Schou, J., Couvidat, S., Bush, R. I., ...
 314 Zhao, X. (2012, July). Comparison of Line-of-Sight Magnetograms Taken by
 315 the Solar Dynamics Observatory/Helioseismic and Magnetic Imager and Solar
 316 and Heliospheric Observatory/Michelson Doppler Imager. *Sol. Phys.*, *279*(1),
 317 295-316. doi: 10.1007/s11207-012-9976-x
- 318 Pedregosa, F., Varoquaux, G., Gramfort, A., Michel, V., Thirion, B., Grisel, O., ...
 319 Duchesnay, E. (2011). Scikit-learn: Machine learning in Python. *Journal of*
 320 *Machine Learning Research*, *12*, 2825-2830.
- 321 Pevtsov, A. A., Bertello, L., Nagovitsyn, Y. A., Tlatov, A. G., & Pipin, V. V. (2021,
 322 January). Long-term studies of photospheric magnetic fields on the Sun. *Jour-*
 323 *nal of Space Weather and Space Climate*, *11*, 4. doi: 10.1051/swsc/2020069
- 324 Scherrer, P. H., Bogart, R. S., Bush, R. I., Hoeksema, J. T., Kosovichev, A. G.,
 325 Schou, J., ... MDI Engineering Team (1995, December). The Solar Oscilla-
 326 tions Investigation - Michelson Doppler Imager. *Sol. Phys.*, *162*(1-2), 129-188.
 327 doi: 10.1007/BF00733429
- 328 Scherrer, P. H., Schou, J., Bush, R. I., Kosovichev, A. G., Bogart, R. S., Hoeksema,
 329 J. T., ... Tomczyk, S. (2012, Jan). The Helioseismic and Magnetic Imager
 330 (HMI) Investigation for the Solar Dynamics Observatory (SDO). *Sol. Phys.*,
 331 *275*, 207-227. doi: 10.1007/s11207-011-9834-2
- 332 Seabold, S., & Perktold, J. (2010). statsmodels: Econometric and statistical model-
 333 ing with python. In *9th python in science conference*.
- 334 Tanaka, H., Castelli, J. P., Covington, A. E., Krüger, A., Landecker, T. L.,
 335 & Tlamicha, A. (1973, March). Absolute Calibration of Solar Radio
 336 Flux Density in the Microwave Region. *Sol. Phys.*, *29*(1), 243-262. doi:
 337 10.1007/BF00153452
- 338 Tapping, K. F. (2013, July). The 10.7 cm solar radio flux (F_{10.7}). *Space Weather*,
 339 *11*(7), 394-406. doi: 10.1002/swe.20064
- 340 Tiwari, S. K., Thalmann, J. K., Panesar, N. K., Moore, R. L., & Winebarger, A. R.
 341 (2017, July). New Evidence that Magnetoconvection Drives Solar-Stellar

- 342 Coronal Heating. *ApJ*, *843*(2), L20. doi: 10.3847/2041-8213/aa794c
- 343 Upton, L. A., & Hathaway, D. H. (2014a, September). Effects of Meridional Flow
344 Variations on Solar Cycles 23 and 24. *ApJ*, *792*(2), 142. doi: 10.1088/0004-
345 -637X/792/2/142
- 346 Upton, L. A., & Hathaway, D. H. (2014b, January). Predicting the Sun's Polar Mag-
347 netic Fields with a Surface Flux Transport Model. *ApJ*, *780*(1), 5. doi: 10
348 .1088/0004-637X/780/1/5
- 349 Upton, L. A., & Hathaway, D. H. (2018, August). An Updated Solar Cycle 25 Pre-
350 diction With AFT: The Modern Minimum. *Geophys. Res. Lett.*, *45*(16), 8091-
351 8095. doi: 10.1029/2018GL078387
- 352 Warren, H. P., Emmert, J. T., & Crump, N. A. (2017, August). Linear forecasting
353 of the F_{10.7} proxy for solar activity. *Space Weather*, *15*(8), 1039-1051. doi: 10
354 .1002/2017SW001637
- 355 Woods, T. N., Eparvier, F. G., Hock, R., Jones, A. R., Woodraska, D., Judge, D.,
356 ... Viereck, R. (2012, Jan). Extreme Ultraviolet Variability Experiment
357 (EVE) on the Solar Dynamics Observatory (SDO): Overview of Science Objec-
358 tives, Instrument Design, Data Products, and Model Developments. *Sol. Phys.*,
359 *275*(1-2), 115-143. doi: 10.1007/s11207-009-9487-6
- 360 Yeo, K. L., Feller, A., Solanki, S. K., Couvidat, S., Danilovic, S., & Krivova, N. A.
361 (2014, January). Point spread function of SDO/HMI and the effects of stray
362 light correction on the apparent properties of solar surface phenomena. *A&A*,
363 *561*, A22. doi: 10.1051/0004-6361/201322502